

# **Towards an Understanding of Ligand Induced Functional Conformational Changes of MexB Efflux Transporter**

Shirin Jamshidi<sup>†</sup>, J. Mark Sutton<sup>‡</sup>, Sara Jambarsang<sup>‡</sup> and Khondaker Miraz Rahman<sup>†\*</sup>

<sup>†</sup>Institute of Pharmaceutical Science, School of Cancer and Pharmaceutical Sciences, King's College London, Franklin-Wilkins Building, 150 Stamford Street, London, SE1 9NH, UK

<sup>‡</sup>Public Health England, National Infection Service, Porton Down, Salisbury, Wiltshire, SP4 0JG, UK

<sup>‡</sup>Department of Biostatistics and Epidemiology, School of Public Health, Sadoughi University of Medical Sciences, Yazd, IR

\*Corresponding author: k.miraz.rahman@kcl.ac.uk

## **Abstract**

In this study, we evaluate the ligand-induced structural rearrangements and conformational changes of MexB, in relation to the protonation state of critical acidic residues, using tetracycline (TET) as a model substrate and phenylalanine-arginine beta-naphthylamide (PAβN) as a model inhibitor.. We find that ligand binding leads to significant differences in the functional motions of transmembrane helices in conjunction with the multi-binding site. Ligand binding and subsequent extrusion or inhibition events are the consequence of various conformational changes in pump structure. Substrate binding affects conformational changes in a way that promotes the switching mechanism and efflux process. In contrast, inhibitor binding disturbs the switching mechanism and inhibits the pump by prompting different conformational changes in the protein structure. This study suggests that the Asp566 residue plays a critical role in the rearrangement of the transmembrane domains in the ligand-bound state.

## **Keywords**

MexB efflux pump transporter, molecular dynamics simulations, conformational changes, Ligand binding, phenylalanyl-arginine-beta-naphthylamide, tetracycline.

## Introduction

*Pseudomonas aeruginosa* is a major opportunistic pathogen and a leading cause of hospital-acquired infections and mortality worldwide<sup>1</sup>. It displays notable degrees of intrinsic resistance to a wide variety of antimicrobial agents, including most  $\beta$ -lactams, tetracyclines, chloramphenicol and fluoroquinolones. Efflux pumps present in *P. aeruginosa* play a significant role in conferring this resistance upon the bacterium<sup>2-7</sup>. Overexpression of RND (Resistance-Nodulation-Division) superfamily efflux pumps in Gram-negative bacteria is a primary component of multidrug resistance (MDR)<sup>8</sup>. This type of efflux pumps recognizes a diverse range of compounds and harness the proton-motive force (PMF) to pump them out of the bacterial cell. MexAB-OprM, an RND-type efflux pump, is one of the major efflux pumps that operate in *P. aeruginosa* and confer resistance to antimicrobials<sup>9</sup>. It is a tripartite pump consisting of an inner membrane spanning transporter MexB, a trimeric lipoprotein OprM that associates with outer membrane and a hexameric membrane fusion protein MexA that forms a stable complex with MexB at the inner membrane<sup>6</sup>. The MexB subunit is a large protein with a molecular mass of 113 kDa and has 1,046 amino acid residues. It consists of a transmembrane domain, a porter domain and a funnel-like (FL) domain. The transmembrane domain has 12  $\alpha$ -helices and the porter domain contains the drug-binding site while the FL domain interacts with other components of the transporter<sup>10-12</sup>. The large loop like structures present in MexB interacts with both MexA and OprM to form the functional pump assembly<sup>13-17</sup>. The transmembrane domain contains five charged amino acid residues and three out of these five residues are highly conserved in RND superfamily of efflux pumps. The specific location of these highly conserved charged residues in the transmembrane domain suggests important role of these residues in proton conduction<sup>11</sup>.

The substrate specificity and selectivity of the MexAB-TolC efflux pump depends on the homotrimeric structure of MexB. It has a threefold asymmetric conformation in which each monomer adopts a different conformation (access, binding or extrusion)<sup>18-24</sup> and employs an allosterically coupled rotation mechanism wherein each monomer successively adopts one of the three aforementioned conformations<sup>20,21,24-30</sup>. The proximal and distal binding pockets that are involved in forming the multi-binding site of MexB play critical roles in determining its substrate specificity and binding<sup>31-40</sup>. The distal binding pocket includes many hydrophobic, polar and charged residues, and this microenvironment mediates the extrusion of a wide range of compounds by RND superfamily pumps<sup>41-43</sup>.

Using X-ray crystallography and computational simulations, Eicher and coworkers<sup>44</sup> showed a collective motion between conformational changes of the transmembrane domain for protons and pore domain at the periplasmic area for ligands in three protomers of main components of RND efflux pump, AcrB<sup>44</sup>. The mechanism of proton-coupled drug-efflux in RND superfamily transporters has been described as the collective motion. In this study, by considering the same protonation states of the specific residues of the transmembrane domain detailed in the aforementioned study, we show the effect of ligand binding on the conformational changes with the help of principal component analysis (PCA) and by monitoring the density of distances of transmembrane helices in the protomers. We identify several essential motions and functional dynamics and describe the conformational changes that govern distinct access, binding and release states to gain insight into the efflux or inhibition mechanism in the presence of a ligand. The results of this study that connects structural and functional aspects could set the stage for inhibitor and new type of hybrid efflux resistant antibiotic design strategies that can explicitly target mechanistic features of a particular pump.

## Results

**Important regions of MexB.** Table S1 details the residues in MexB that interact with the ligand during MD simulation trajectories. They have been marked by sequence alignment of MexB from *P. aeruginosa* to the solved structure of AcrB from *Escherichia coli*<sup>19,45</sup>. The matched amino acids in the MexB and AcrB sequences occupy the same locations in their corresponding PDB structures. Additionally, the protonated residues in the transmembrane domains<sup>44</sup> of the different monomers of the protein are listed.

**Principal component analysis.** Principal component analysis (PCA) was performed as a post-MD analysis to characterize the conformational transitions in the MexB transporter, modulated by the inhibitor (PA $\beta$ N) and substrate (TET) (Fig. S1). As Fig. 1 indicates, different patterns of conformational changes in the systems revealed different dynamics and functions between the free form of the MexB transporter and the transporter in complex with either the inhibitor or the substrate. Ligand binding clearly affects the conformational changes of the transporter, with different ligands prompting distinct conformational changes.

**Correlation network analysis.** The motions of the residues of the diverse protomers were monitored using the first mode of PCA to understand the essential dynamics for uncovering functional differences and their mechanisms. For the sake of simplicity, they are shown in two graphs which have been categorized differently (Fig. S2 and S3). PCA on MD data was useful for finding the protein segments that were most involved in structural changes. The RMSF (root mean square fluctuations) calculation was used to determine how much each residue moved during the trajectory and how much each residue contributed to a principal component. This enabled us to define a correlation in the motion of the essential parts of the efflux pump after complexing with the ligands was observed. Comparing with other systems,

the fluctuations in the binding monomer of the PA $\beta$ N-bound complex were slightly restricted, especially in critical regions like the tip residue Phe617. However, diverse parts of the protein show a distinct correlation to the tetracycline-bound and ligand-free states of MexB. From the plots in [Fig. S2](#), it can be observed that the access, binding and release protomers are the protomers with the most peak fluctuations in the ligand-free MexB, MexB-PA $\beta$ N and MexB-TET systems, respectively. The highest and lowest functional motions were seen in the access and release protomers, respectively, whilst the binding monomers show the highest degree of correlation among diverse parts of the protein between the different efflux pump systems. Also, considering the peaks of the fluctuations in each of the graphs of the binding protomer, the highest degree of correlation among the different regions can be observed in the MexB-PA $\beta$ N complex, with most peaks in diverse regions of protein, and the lowest correlation belongs to ligand-free MexB, with few peaks on the corresponding graphs ([Fig. S2](#)). However, the various graphs clearly show different dynamics in the different systems and even within protomers of an individual system. These graphs indicate that the G-loop (Phe617) is much more flexible in the binding and release monomers of ligand-free MexB compared to MexB-PA $\beta$ N. The same region also shows considerable fluctuations in the case of MexB-TET ([Fig. S3](#)).

**Distance density distributions:** Substrate and inhibitor binding induce conformations of MexB which are distinct from the free form of the protein., Monitoring the distances between protonating residues in transmembrane helices, during MD simulations, was transformed into distance density distributions which characterize the spatial relationships between pairs of transmembrane helices in the diverse protomers of MexB ([Fig. 2](#)). The distances between the protonated residues in each helix of the transmembrane domain (marked below) were

considered to monitor the relative orientation of the helices during conformational changes in different systems.

Also, by considering [Fig. S2 & S3](#), the protomers with highest RMSF in several helices of the transmembrane (TM) domains are represented in [Table S2](#). As shown by the data, the access, release and binding protomers are the protomers with the highest fluctuation and functional dynamics in the ligand-free, PA $\beta$ N-bound, and TET-bound forms of MexB, respectively.

The results show that the distance density peaks between different TMs are clustered in ligand-bound states, compared with the free form of MexB in which the distances showed a broad range of distribution ([Fig. 3](#)). Broad distributions in TM10-11 are observed among diverse protomers with average distances of 18, 58 and 56 Å for access, binding and release protomers, respectively ([Fig. 3, row 5](#)) and in TM2-TM10 among diverse systems with distances of 27, 26 and 29 Å in binding protomers of MexB, MexB-PA $\beta$ N and MexB-TET, respectively. At several sites, the shape of the distributions and the changes induced by different ligand-binding forms suggest equilibrium between multiple states ([Table 1](#)). Further analysis of the data shows patterns which include: i) TM10-TM11 are much closer in access protomers, ii) the turn connecting TM7 (TM7t) is closer to binding site in ligand binding state in access protomers, iii) TM7t-TM10 are closer in binding monomers, and finally, iv) TM2-TM10 and TM4-TM10 are closer in release protomers of the systems.

As observed in the PCA analysis ([Fig. 1](#)), conformational changes are affected by ligand binding. Here again, comparison of the crystal and ligand-free distance distributions with those of the ligand-bound structures reveals considerable differences in structural changes upon the binding of different ligands. These are primarily observed at i) TM4 and TM10 ([Fig. 3, row 4](#)), which are directly involved in functional dynamics of the protein as the central

148 helices of the transmembrane domains, at ii) TM2 and TM11 (Fig. 3, row 2), which border the  
149 bilayer, and finally iii) the turn connecting TM7 (TM7t) and TM10 (Fig. 3, row 7). TM7t includes  
150 key residues involved in transferring functional dynamics between the transmembrane  
151 domains and pore domains that includes the multi-binding site. Importantly, diverse pairs of  
152 TMs helices represented in Fig. 3, include the protonated residues that are essential to the  
153 proton translocation function of the transporter as a proton motive force nanomachine.

154 In contrast, minor rearrangements along the interface of TM4 and TM11 are observed in the  
155 density distance distributions (Fig. 3, row 3). Significant changes in the distances with the  
156 largest density and the width of the distance distributions are observed along with the turn  
157 connecting TM7 (includes key residues of Asp566). Most substantial changes occurred at  
158 TM10-TM11 (Fig. 3, row 8) with restricted mobility observed in almost all the monitored helix-  
159 helix interfaces. Therefore, we consider that these distance changes reflect functional  
160 dynamics of diverse conformations, that proceed by a rearrangement of the TM helices that  
161 starts from the turn connecting TM7t end to TM11. The whole path of dynamics proceeds by  
162 ligand binding that affects the distal binding site conformational changes, by rearrangement  
163 of the location of G-loop and then Ser loop that finally transfers to TM7t. This path can  
164 happen, conversely, from the distal site by ligand binding to the transmembrane domain *via*  
165 the turn, including Asp566.

166 Density maps of distances, represented in Fig. 3, confirm the extensive ligand-dependent  
167 rearrangements in the complex structures. In particular, the lowest monitored distance  
168 around 8 Å between amino acid Asp566 of TM7t from Asp923 of TM10 (Fig. 3, row 7) suggests  
169 an essential role for binding monomers in the conformational changes toward the function of  
170 the efflux pump. Notably, ligand binding restrains the distance distributions (Fig. 3). Also as  
171 represented in Fig. S4, the average distances involving Asp566 show more variety than the

monitored averages for other amino acids. This indicates the effect of ligand binding on the location and orientation of Asp566 to Asp923 and, consequently, the rearrangement of the turn connecting TM7 and TM10 with respect to each other. [Table 1](#) clearly shows the density of distance between TM7t and the binding site is slightly farther (22.04, 22.55 and 22.78 Å in ligand-free, PAβN-bound and TET-bound MexB, respectively) whereas the distance between TM7t and TM10 is slightly closer in the binding monomer of ligand-bound systems (8.74 and 8.55 Å in PAβN-bound and TET-bound MexB, respectively) compared with the ligand-free system (8.75 Å). It can lead to rearrangements along the rest of the TM helices. The different natures of the rearrangements along the various TM helices of the systems reflects the effect of ligand binding and the type of ligand. Consistent with this conclusion, the density of distance distributions when the system is ligand-free are broad, suggesting greater flexibility of the backbone. Substantial amplitude distance changes are observed in TM2-TM10 and TM2-TM11 (Fig. 3, rows 1 and 2), indicating extensive ligand-dependent repacking.

Although the exact nature of the underlying structural rearrangements is challenging to infer from the data, distance densities suggest a flow of conformational rearrangement among the TM helices with a central role of Lys939 (TM10), Thr976 (TM11) and Asp407 and Asp408 (TM4) in conferring conformational changes, promoted by ligand binding in the multi-binding site of the transporter. This agrees with previous observations by Takatsuka and Nikaido that Thr978, Lys940, Asp407 and Asp408 in AcrB are essential to adopt conformational changes towards the functional dynamic of the transporter <sup>46</sup>. Also, according to the current study, Asp407 or Asp408 of TM4 and Lys939 of TM10 show short distance components to Thr976 of TM11 in the ligand-free and ligand-bound states ([Fig. 3](#) and [Table 1](#)). Conversely, the lower density and/or broader range of distance in the ligand-free distributions (Fig. 3) suggest a highly flexible conformation with extensive fluctuations, that is in a good agreement with



196 RMSF graphs (Fig. S2 and S3). Specifically, more fluctuations are seen within the TM helices  
197 and multi binding site regions in ligand-free form compared with ligand-bound systems.

198 The penetration of Asp566 toward TM10, implied by the shorter distance compared with the  
199 ligand-free state, presumably confers the conformational changes in transmembrane  
200 domains in different ways in PA $\beta$ N-bound and TET-bound systems. The domain including the  
201 G-loop is connected to Asp566 through a super secondary structure of beta-alpha-beta motifs  
202 that has a crucial role in forming the hydrophobic core of the pump. Binding of ligands to the  
203 protein causes Asp566 to undergo a closing motion upon ligand binding, evidenced by the  
204 shift in the density of distance (Fig. S5). In the next stage, ligand binding affects  
205 transmembrane conformational changes by the proximity of Asp566 to Asp923 which are  
206 protonating residues in TM7t and TM10 respectively.

207 However, the density distributions at sites containing of Asp566 and Asp923 show the  
208 presence of a trend of focusing and reducing distance. This movement is attenuated near the  
209 end of the TM10 helix. Except for the distance between Asp566 and Asp923 in TM7t-TM10 of  
210 the binding protomer, most of the distances in the transmembrane domains were  
211 characterized by broad distributions, indicating a highly dynamic backbone (Figs. S2 and S3).

212 The conformation is stabilized by ligand binding and is slightly reduced in MexB-PA $\beta$ N with  
213 greater correlation between different regions of the transporter. Phe617 is in direct contact  
214 with the bound ligand in the complex structures during MD trajectories. Moreover, the G-  
215 loop forms part of a hydrophobic groove, on one side, and it is involved in inhibition by  
216 affecting Asp566 location through the beta-alpha-beta motif connection on the other side.

217 Asp566, can be identified as a critical residue linking the ligand-binding conformational  
218 changes to the transmembrane domains, and the other key residues in the multi-binding site  
219 by monitoring the distance density between Asp566, and the other key residues in the multi-

220 binding site (Fig. 4). Notably, Asp566 shows a broader range of distance density to the multi-  
221 binding site residues in the access protomer compared to the binding and release protomers.  
222 Also, it was observed that the graphs of ligand-bound states in diverse monomers showed  
223 more variety, when compared to each other, than those in a ligand-free state. This likely  
224 reflects the direct effect of ligand binding on conformational dynamics.

225 Monitoring the distance between the ligand and the key residues of the passageway in the  
226 multi-binding site in different complex systems (Fig. 5) shows that the range of density  
227 distributions are broader in the MexB-PA $\beta$ N complex compared with the MexB-TET complex.  
228 The density of distances is restricted to a certain value in the MexB-TET complex, which is  
229 larger than the corresponding values in the case of MexB-PA $\beta$ N complex. It clearly shows that  
230 PA $\beta$ N, as mentioned above, could occlude the passageway and could affect the  
231 conformational changes of MexB in a way that means the conformer switching mechanism is  
232 distorted more than for tetracycline binding. This result is in accordance with the PCA analysis  
233 (Fig. 1) in which the graphs of conformational changes in the TET-bound complex is more  
234 similar to the ligand-free system than the PA $\beta$ N-bound one.

235

236

237 Also, monitoring the distance between the residues forming the proposed gate and cleft (Fig.  
238 6) showed that ligand binding significantly affects the distance density in ligand-bound states  
239 compared with the ligand-free form. The access, binding and release monomers confer  
240 diverse density with different pattern in the distance between cleft and postulated gate  
241 residues. According to the graph, PA $\beta$ N binding gives a broader range of change with almost  
242 same values in the distance range of ligand free form but still noticeable difference in density

distribution in binding and access protomers whereas TET binding decreases the range in binding and shifts the range toward higher values in release protomer considerably.

To investigate the MexB structure under ligand binding conditions that are expected to promote diverse conformations, we compared the highest points of distance density distributions, represented in Table 1, to the corresponding distances in the crystal structure of MexB (Protein Data Bank identity code 3W9) and MD simulated ligand-free form separately (Fig. S6). The crystal structure was considered to provide a general reference for the conformation, so the right panels were assigned as the reference to monitor and compare the discrepancy of the distance density with certain distances in the crystal structure. As the left panel shows, the graphs for release protomers are almost superimposable and aligned with each other. However, there is a considerable difference between two complexes when the binding and access protomers are considered. The discrepancy remains after subtracting the references, clearly showing that ligand binding could lead to a specific dynamic function that results in efflux in the case of the substrate and inhibition in the case of the inhibitor.

It seems that differences in protonation states of specific residues in the access and release protomers could efficiently drive the conformational changes in the monomers by adjusting the distances between the TM helices and affecting their orientations to each other. The differences in conformational changes in binding and access protomers, despite the similar protonation state in certain residues, confirms the key role of ligand binding on TM helices repacking and its role in consequent conformational changes. Protonation invariably leads to discrepancy among TM helices in the diverse protomers of the different systems. Therefore, different rearrangement in the transmembrane domains of the transporter occur because of the ligand binding.

Distance density distributions of helices TM2, TM10, TM4 and TM11 in the binding protomers suggest that TM10 and TM11 undergo rearrangement of the transmembrane domain when a ligand is bound. The TM4 and TM10 rearrangements are promoted by ligand binding and likely facilitated by the protonation state in Asp407 and Asp408. These residues tend to take a proton from Lys939 at TM11 which leads to changes in the conformational dynamics of the corresponding TM helices in binding and access monomers. The conformational changes at the binding site extend to the loop connecting TM7, linking it to the TM helices.

The right panels of [Fig. S6](#) in the linear view ([Fig. S7](#)) indicate a significant shortening in the intra-residue differences in the binding protomer of MexB-PA $\beta$ N (e.g. 1, 2, 3, 4, 14, 19, 20, 25, 27, 29 and 47) that imply a large-scale movement of the helices. This is an indicator for occlusion of the transmembrane domain and binding site in the presence of the inhibitor. Although prominent ligand-induced changes in the distance distributions are observed in the transmembrane domains of TM2, TM10, TM4 and TM11, they are generally smaller in magnitude and no discernible pattern was evident from the comparison of changes in other helices. Given that these TMs are involved in conformational changes and consequently function, it is not surprising that the rearrangements of TM helices with specific protonated residues, necessitate rearrangement at the transmembrane domains.

Overall, the density distributions reveal several trends consistent with three distinct conformations corresponding to the inhibitor-bound, substrate-bound, and ligand-free MexB complexes. First, we can observe changes in the distance density as well as the width of the density distributions between the diverse conditions which unequivocally demonstrate extensive conformational rearrangements. Second, the shape of these distributions implies that the substrate-bound and inhibitor-bound states are ordered in stark contrast with each

291 other and with the highly dynamic ligand-free state, with a broader range in the distribution  
292 values. The ligand-free form of MexB shows a wide range of density distances, that it is much  
293 more restrained, or which shows a higher density in ligand-bound states of MexB. Also, the  
294 effect of ligand binding is considerable in the distances between TM helices of MexB in the  
295 different systems after extracting them from long MD simulations trajectories.

296

## 297 **Discussion**

298 To provide a global perspective on the conformational changes and structural  
299 rearrangements of MexB, the changes in the distance density were plotted as a function of  
300 the distances. It has been narrowed down to monitor just the critical residues belonging to  
301 the essential regions of the protein that were expected to be involved in functional dynamics.  
302 Nevertheless, this exercise provides the qualitative visualization of the regions of  
303 conformational change, thereby identifying a complex web of structural rearrangements  
304 focused on TM2, TM4, TM10 and TM11 and the turn connecting to TM7. The ligand-free form  
305 of MexB has been considered as a reference to interpret the diverse analysis in a structural  
306 context. The data showed extensive differences between the ligand-free and the ligand-  
307 bound complex conformations in MexB.

308

309 In this study, we have gained insight into the differential function of MexB in the presence of  
310 substrates and inhibitors. The results show that ligands induce motion in the transporter  
311 through their interactions with the multi-binding site, but that this motion is ligand-  
312 dependent and thus different for substrates and inhibitors. To this end, the conformer  
313 patterns adopted by the TET-bound form are not observed in the simulations of the PA $\beta$ N-  
314 bound transporter. This type of motion dependency has implications for understanding the  
315 effects of conformational changes on ligand binding by MexB and in defining how inhibitors  
316 mediate their effects.

317

318 Ligand binding affects the rotation and tilting of TM4–TM10, TM2, and TM11, which together  
319 modulate either the efflux or the inhibition pathway. Asp566 which is in the TM7 connecting  
320 loop between the binding site and transmembrane helices, emerges as a central amino acid

residue in this conformation switch, undergoing extensive rearrangement in diverse protomers. The importance of Asp566 to the conformational switch was confirmed, acting primarily through extensive rearrangement of TM2, TM4, TM10 and TM11.

The flexibility of Asp566, presumably a consequence of the ligand binding, enables large-scale reconfiguration upon concurrent ligand binding and protonation of Asp566. The rearrangements of the backbone and side chains of TM helices may lead to a different conformational change, consequently resulting in a different function. Ligand binding induce the rearrangement of the TM helices, which participate in the functional mechanism. TM helices undergo significant amplitude movement coupled to extensive rearrangement of the transmembrane domain. This movement is controlled both by the diverse protonation state of Asp407, Asp508, Asp566 and His338 in diverse protomers and the type of ligand bound simultaneously.

In brief, this study showed that ligand binding extensively affects the conformational changes leading to a specific dynamic of the MexB transporter that results in either efflux or pump inhibition. The results of this study include detailed data on the atomic level that could help elucidate the mechanism of action of tripartite efflux pumps and consequently inform the development of better inhibitors of RND efflux pumps by rational drug design, in turn helping to overcome antibiotic resistance in multidrug-resistant Gram-negative pathogens.

## Methods

MD simulations were performed using the program AMBER 16 package program<sup>47</sup>. MD simulations started from the docked structures, obtained from blind docking by AutoDock SMINA, which followed by flexible docking using the GOLD<sup>48</sup> program. In this study, the power of GPU acceleration was used to study conformational transitions that occur in MexB in free form and interaction with substrate and inhibitor, separately. Also, the CUDA implementation of PMEMD was used to carry out the simulations on GPUs.

**System setup.** The crystallographic structure of *Pseudomonas aeruginosa* MexB transporter was obtained from Protein Data Bank (PDB ID code 3W9I with a resolution of 2.71 Å<sup>49</sup> in the Loose/Tight/Open (LTO) asymmetric conformation as the starting conformation for the study. The residues not resolved by x-ray were added to amend the structure using Biovia Accelrys Discovery Studio. The most probable protonation state of specific residues in the access (Loose/L) - binding (Tight/T) - release (Open/O) transition was changed. These include Asp407 and Asp408, in the core of the TM domain, which is ionized in the L and T states but becomes protonated in the O state. Interestingly, His338 at the periplasmic end of TM2 is protonated in the O state and becomes deprotonated in L and T states whereas Asp923 at the periplasmic end of TM10 is protonated in L and T states and becomes deprotonated in the O state; conversely, the neighbouring Asp566 in the region between TM7 and PC1 subdomain is most likely deprotonated in L and T and becomes protonated in the O state (Fig. S6). The previous calculations indicated that both Lys939, Arg971, and Asp976 remain protonated throughout the cycle. All these residues were adjusted to their protonation or deprotonated states in the corresponding protomer in the PDB crystal structure of MexB by following the literature<sup>44</sup>. The final structure was equilibrated and minimized using AMBER 16 package program.



Phenylalanyl-arginine- $\beta$ -naphthylamide (PA $\beta$ N) and tetracycline (TET) (Fig. S1) PDB structures were generated by Chem3D 15.0 and were minimized using SYBYL software program. The force-field parameters for the ligands were developed following the Antech AMBER protocol of the AMBER package program.

**Molecular docking.** The starting structures for running simulations were obtained by molecular docking of the ligands to the MexB transporter. The orientation of the ligands within the multi-binding site of the binding protomer was taken from docking calculations performed with the AutoDock SMINA package through blind molecular docking, to find the particular cavity for ligands within the multi-binding site of the transporter with the best affinity among all the probable ones. All the parameters were kept at their default values for running SMINA. Then, an evaluated flexible molecular docking was performed using GOLD molecular docking into the SMINA-located binding site to find the best pose and orientation of the ligands in the located binding pocket. The Genetic algorithm (GA) is used in GOLD ligand docking to examine the ligand conformational flexibility, along with the partial flexibility of the protein. The maximum number of runs was set to 20 for each compound, with the default parameters (100 population size, 5 for the number of islands, 100,000 number of operations and 2 for the niche size). Default cut off values of 2.5Å (dH-X) for hydrogen bonds, and 4.0 Å for van-der-Waals distance was used. When the solutions attained RMSD values within 1.5 Å, GA docking was terminated.

**Molecular dynamics simulations.** MD simulations of the free form and ligand-bound structures of MexB were carried out using the AMBER16 package program<sup>47,50</sup>. The topology and the initial coordinate files for these apo-protein structures were created using the LEaP

391 module of AmberTools16 ToolKit program. The protein and docked complexes were  
392 successively embedded in 1-palmitoyl-2-oleoyl-sn-glycerol-3 phosphoethanolamine (POPE)  
393 bilayer patches, solvated with explicit TIP3P water model and neutralized with the required  
394 number of randomly placed K<sup>+</sup> ion. The ion count was suitably adjusted to account for an  
395 osmolarity of 0.15 M KCl. Embedding of the protein systems into a pre-equilibrated POPE  
396 bilayer patch was performed using the PPM server and subsequently the CharmmGUI tool <sup>51</sup>.  
397 The lipid residue nomenclature was converted from the CHARMM to AMBER format using the  
398 charmm lipid2amber.py python script provided with AmberTools. The central pore lipids were  
399 then added after calculating the number of lipids to be added to each leaflet by dividing the  
400 approximate area of the central pore by the standard area per lipid of POPE molecules <sup>52</sup>.  
401 Periodic boundary conditions were used, and the calculated box dimensions from the water  
402 molecules were 162.17×162.67×197.35.

403 For running molecular dynamics of lipid bilayer systems, including protein complexes, the  
404 following protocol was used in an order; Minimization, heating 1 (holding the lipids fixed),  
405 heating 2 (holding the lipids fixed), 10X Hold to equilibrate periodic box dimensions,  
406 production with constant pressure. Energy minimization with a combination of steepest  
407 descent and conjugate gradient methods was carried out using the pmemd program  
408 implemented in AMBER16 to relax internal constraints of the systems by gradually releasing  
409 positional restraints. All the systems were minimized for 15000 cycles of steepest descent  
410 followed by 15000 cycles of conjugate gradient minimization. Following this, the systems  
411 were heated from 0 to 303 K by a 1 ns heating (0–100 K) under constant volume (NVT)  
412 followed by 5 ns of constant pressure heating (NPT) (100–303 K) with the phosphorous heads  
413 of lipids restrained along the z-axis to allow membrane merging and to bring the atmospheric  
414 pressure of the system to 1 bar. Langevin thermostat, with a collision frequency of 1 ps<sup>-1</sup>,

was used to maintain a constant temperature, and multiple short equilibration steps of 500ps under anisotropic pressure scaling (Berendsen barostat) in NPT conditions were performed to equilibrate the box dimensions. A time step of 2 fs was used during all these runs, while post-equilibrium MD simulations were carried out with a time step of 2 fs under constant volume conditions after hydrogen mass repartitioning<sup>53</sup>. The particle-mesh Ewald (PME) algorithm was used to evaluate long-range electrostatic forces with a non-bonded cutoff of 10 Å. During the MD simulations, the length of all R–H bonds were constrained with the SHAKE algorithm. The ff14SB<sup>54</sup> version of the all-atom Amber force field was used to represent the protein systems, while lipid16<sup>52</sup> parameters were used for the POPE bilayer. After equilibration, 2μs long MD simulations were performed for each system. Trajectory analysis was done using cpptraj module of AmberTools16, Bio3D, and VMD1.9.1, and density graphs were plotted using the R program.

**Principal component analysis.** To identify and highlight possible identities and differences in the collective motions of protomers, we determined the covariance matrices from the equilibrium trajectory and conducted a principal component analysis<sup>55,56</sup>. As conventional in principal component analysis, the covariance matrix was developed utilizing the three-dimensional positional fluctuations of Cα atoms from their ensemble average position (after least-squares fitting to eliminate rotational and translational motion). Diagonalization of the covariance matrix produces a collection of eigenvectors and corresponding eigenvalues, which describe the direction and amplitude of the motion, respectively. The eigenvectors are then sorted according to the decreasing order of their associated eigenvalues, such that the first eigenvector describes the most substantial contribution to the total fluctuation of the system. To visualize the motions represented by the eigenvectors, the structures from the

trajectories can be projected onto each eigenvector of interest (principal component or PC) and transformed back into Cartesian coordinates. The two extreme projections along each eigenvector can then be interpolated to create an animation or compared to understand which parts of the protein are moving according to that specific eigenvector and to what extent. Usually, a combination of the first few principal components can represent most of the collective motions, the “essential dynamics”<sup>55</sup>, occurring in an MD simulation among the different regions of a protein. This method has the benefit that the dynamics along the individual modes can be inspected and visualized separately, thereby allowing one to filter the main modes of collective motion from more local fluctuations.

**Clustering of MD trajectories.** For cluster analysis of the MD trajectories, the average-linkage hierarchical agglomerative clustering method implemented in *cpptraj* module of AMBER was used. Such clustering serves to decrease the number of structures for analysis, yet maintaining the large conformational space sampled during the MD runs. In this approach, for each system, the representative structures from each of the 10 top clusters produced were used to conduct quantitative analyses in order to account for dynamical behaviour.

**Analysis of protein conformational change using principal component analysis (PCA).** The original trajectory files produced by MD were significantly large, and we cannot include them in the Bio3D package installed in the R program due to space limitations, so the trajectories in each MD simulations were down-sampled with an interval of 50. The points represented in the conformer plots were computationally clustered and coloured by the cluster. This was performed by creating a distance matrix of the principal components of interest.

PCA reduces the dimensionality of large data sets by calculating a covariance matrix and its eigenvectors. Vectors with the highest eigenvalues become the most significant principal components. When principal components are plotted against each other, similar structures cluster, each cluster then theoretically represents a different protein conformational state. To avoid sample noise from random fluctuations<sup>57,58</sup>, following MD simulations of the MexB transporter systems, the PCA was calculated only for C $\alpha$  atoms. Then, each protomer was selected in a separate PCA analysis, which was a good discriminator of conformations. With the Bio3D package installed in R, the plot command has been overloaded to create a default PCA plot with four graphs. Three are the z-scores of the first three principal components plotted against each other in two dimensions. The last is a scree plot representing how much of the variance of the data set is captured by each principal component.

## References

- 1 Brown, M. R. W. Resistance of *Pseudomonas aeruginosa*. doi:<http://doi.org/10.1002/jobm.19770170412> (1975).
- 2 Kohler, T. *et al.* Multidrug efflux in intrinsic resistance to trimethoprim and sulfamethoxazole in *Pseudomonas aeruginosa*. *Antimicrob Agents Chemother* **40**, 2288-2290 (1996).
- 3 Li, X. Z., Nikaido, H. & Poole, K. Role of mexA-mexB-oprM in antibiotic efflux in *Pseudomonas aeruginosa*. *Antimicrob Agents Chemother* **39**, 1948-1953, doi:10.1128/aac.39.9.1948 (1995).
- 4 Li, X. Z., Zhang, L., Srikumar, R. & Poole, K. Beta-lactamase inhibitors are substrates for the multidrug efflux pumps of *Pseudomonas aeruginosa*. *Antimicrob Agents Chemother* **42**, 399-403 (1998).
- 5 Masuda, N. & Ohya, S. Cross-resistance to meropenem, cephems, and quinolones in *Pseudomonas aeruginosa*. *Antimicrob Agents Chemother* **36**, 1847-1851, doi:10.1128/aac.36.9.1847 (1992).
- 6 Poole, K., Krebs, K., McNally, C. & Neshat, S. Multiple antibiotic resistance in *Pseudomonas aeruginosa*: evidence for involvement of an efflux operon. *J Bacteriol* **175**, 7363-7372, doi:10.1128/jb.175.22.7363-7372.1993 (1993).

493 7 Rella, M. & Haas, D. Resistance of *Pseudomonas aeruginosa* PAO to nalidixic acid and  
494 low levels of beta-lactam antibiotics: mapping of chromosomal genes. *Antimicrob*  
495 *Agents Chemother* **22**, 242-249, doi:10.1128/aac.22.2.242 (1982).

496 8 Li, X. Z., Plesiat, P. & Nikaido, H. The challenge of efflux-mediated antibiotic  
497 resistance in Gram-negative bacteria. *Clin Microbiol Rev* **28**, 337-418,  
498 doi:10.1128/CMR.00117-14 (2015).

499 9 Poole, K. Multidrug efflux pumps and antimicrobial resistance in *Pseudomonas*  
500 *aeruginosa* and related organisms. *J Mol Microbiol Biotechnol* **3**, 255-264 (2001).

501 10 Paulsen, I. T., Brown, M. H. & Skurray, R. A. Proton-dependent multidrug efflux  
502 systems. *Microbiol Rev* **60**, 575-608 (1996).

503 11 Guan, L., Ehrmann, M., Yoneyama, H. & Nakae, T. Membrane topology of the  
504 xenobiotic-exporting subunit, MexB, of the MexA,B-OprM extrusion pump in  
505 *Pseudomonas aeruginosa*. *J Biol Chem* **274**, 10517-10522,  
506 doi:10.1074/jbc.274.15.10517 (1999).

507 12 Tseng, T. T. *et al.* The RND permease superfamily: an ancient, ubiquitous and diverse  
508 family that includes human disease and development proteins. *J Mol Microbiol*  
509 *Biotechnol* **1**, 107-125 (1999).

510 13 Ma, D., Cook, D. N., Hearst, J. E. & Nikaido, H. Efflux pumps and drug resistance in  
511 gram-negative bacteria. *Trends Microbiol* **2**, 489-493 (1994).

512 14 Nikaido, H. Prevention of drug access to bacterial targets: permeability barriers and  
513 active efflux. *Science* **264**, 382-388, doi:10.1126/science.8153625 (1994).

514 15 Saier, M. H., Jr., Tam, R., Reizer, A. & Reizer, J. Two novel families of bacterial  
515 membrane proteins concerned with nodulation, cell division and transport. *Mol*  
516 *Microbiol* **11**, 841-847 (1994).

517 16 Nakae, T. Role of membrane permeability in determining antibiotic resistance in  
518 *Pseudomonas aeruginosa*. *Microbiol Immunol* **39**, 221-229 (1995).

519 17 Nakajima, A., Sugimoto, Y., Yoneyama, H. & Nakae, T. Localization of the outer  
520 membrane subunit OprM of resistance-nodulation-cell division family  
521 multicomponent efflux pump in *Pseudomonas aeruginosa*. *J Biol Chem* **275**, 30064-  
522 30068, doi:10.1074/jbc.M005742200 (2000).

523 18 Ma, D. *et al.* Molecular cloning and characterization of *acrA* and *acrE* genes of  
524 *Escherichia coli*. *J Bacteriol* **175**, 6299-6313 (1993).

525 19 Murakami, S., Nakashima, R., Yamashita, E. & Yamaguchi, A. Crystal structure of  
526 bacterial multidrug efflux transporter AcrB. *Nature* **419**, 587-593,  
527 doi:10.1038/nature01050 (2002).

528 20 Murakami, S., Nakashima, R., Yamashita, E., Matsumoto, T. & Yamaguchi, A. Crystal  
529 structures of a multidrug transporter reveal a functionally rotating mechanism.  
530 *Nature* **443**, 173-179, doi:10.1038/nature05076 (2006).

531 21 Du, D. *et al.* Structure of the AcrAB-TolC multidrug efflux pump. *Nature* **509**, 512-  
532 515, doi:10.1038/nature13205 (2014).

533 22 Seeger, M. A. *et al.* Structural asymmetry of AcrB trimer suggests a peristaltic pump  
534 mechanism. *Science* **313**, 1295-1298, doi:10.1126/science.1131542 (2006).

535 23 Sennhauser, G., Amstutz, P., Briand, C., Storchenegger, O. & Grutter, M. G. Drug  
536 export pathway of multidrug exporter AcrB revealed by DARPin inhibitors. *PLoS Biol*  
537 **5**, e7, doi:10.1371/journal.pbio.0050007 (2007).

538 24 Seeger, M. A. *et al.* Engineered disulfide bonds support the functional rotation  
539 mechanism of multidrug efflux pump AcrB. *Nat Struct Mol Biol* **15**, 199-205,  
540 doi:10.1038/nsmb.1379 (2008).

541 25 Takatsuka, Y. & Nikaido, H. Covalently linked trimer of the AcrB multidrug efflux  
542 pump provides support for the functional rotating mechanism. *J Bacteriol* **191**, 1729-  
543 1737, doi:10.1128/JB.01441-08 (2009).

544 26 Takatsuka, Y. & Nikaido, H. Site-directed disulfide cross-linking shows that cleft  
545 flexibility in the periplasmic domain is needed for the multidrug efflux pump AcrB of  
546 Escherichia coli. *J Bacteriol* **189**, 8677-8684, doi:10.1128/JB.01127-07 (2007).

547 27 Schulz, R., Vargiu, A. V., Collu, F., Kleinekathofer, U. & Ruggerone, P. Functional  
548 rotation of the transporter AcrB: insights into drug extrusion from simulations. *PLoS*  
549 *Comput Biol* **6**, e1000806, doi:10.1371/journal.pcbi.1000806 (2010).

550 28 Yao, X. Q., Kenzaki, H., Murakami, S. & Takada, S. Drug export and allosteric coupling  
551 in a multidrug transporter revealed by molecular simulations. *Nat Commun* **1**, 117,  
552 doi:10.1038/ncomms1116 (2010).

553 29 Tornroth-Horsefield, S. *et al.* Crystal structure of AcrB in complex with a single  
554 transmembrane subunit reveals another twist. *Structure* **15**, 1663-1673,  
555 doi:10.1016/j.str.2007.09.023 (2007).

556 30 Wang, Z. *et al.* An allosteric transport mechanism for the AcrAB-TolC multidrug efflux  
557 pump. *Elife* **6**, doi:10.7554/eLife.24905 (2017).

558 31 Vargiu, A. V. & Nikaido, H. Multidrug binding properties of the AcrB efflux pump  
559 characterized by molecular dynamics simulations. *Proc Natl Acad Sci U S A* **109**,  
560 20637-20642, doi:10.1073/pnas.1218348109 (2012).

561 32 Bohnert, J. A. *et al.* Site-directed mutagenesis reveals putative substrate binding  
562 residues in the Escherichia coli RND efflux pump AcrB. *J Bacteriol* **190**, 8225-8229,  
563 doi:10.1128/JB.00912-08 (2008).

564 33 Bohnert, J. A., Schuster, S., Fahnrich, E., Trittler, R. & Kern, W. V. Altered spectrum of  
565 multidrug resistance associated with a single point mutation in the Escherichia coli  
566 RND-type MDR efflux pump YhiV (MdtF). *J Antimicrob Chemother* **59**, 1216-1222,  
567 doi:10.1093/jac/dkl426 (2007).

568 34 Bohnert, J. A., Karamian, B. & Nikaido, H. Optimized Nile Red efflux assay of AcrAB-  
569 TolC multidrug efflux system shows competition between substrates. *Antimicrob*  
570 *Agents Chemother* **54**, 3770-3775, doi:10.1128/AAC.00620-10 (2010).

571 35 Wehmeier, C., Schuster, S., Fahnrich, E., Kern, W. V. & Bohnert, J. A. Site-directed  
572 mutagenesis reveals amino acid residues in the Escherichia coli RND efflux pump  
573 AcrB that confer macrolide resistance. *Antimicrob Agents Chemother* **53**, 329-330,  
574 doi:10.1128/AAC.00921-08 (2009).

575 36 Vargiu, A. V. *et al.* Effect of the F610A mutation on substrate extrusion in the AcrB  
576 transporter: explanation and rationale by molecular dynamics simulations. *J Am*  
577 *Chem Soc* **133**, 10704-10707, doi:10.1021/ja202666x (2011).

578 37 Nakashima, R., Sakurai, K., Yamasaki, S., Nishino, K. & Yamaguchi, A. Structures of  
579 the multidrug exporter AcrB reveal a proximal multisite drug-binding pocket. *Nature*  
580 **480**, 565-569, doi:10.1038/nature10641 (2011).

581 38 Eicher, T. *et al.* Transport of drugs by the multidrug transporter AcrB involves an  
582 access and a deep binding pocket that are separated by a switch-loop. *Proc Natl*  
583 *Acad Sci U S A* **109**, 5687-5692, doi:10.1073/pnas.1114944109 (2012).

584 39 Yu, E. W., Aires, J. R., McDermott, G. & Nikaido, H. A periplasmic drug-binding site of  
585 the AcrB multidrug efflux pump: a crystallographic and site-directed mutagenesis  
586 study. *J Bacteriol* **187**, 6804-6815, doi:10.1128/JB.187.19.6804-6815.2005 (2005).

587 40 Husain, F. & Nikaido, H. Substrate path in the AcrB multidrug efflux pump of  
588 Escherichia coli. *Mol Microbiol* **78**, 320-330, doi:10.1111/j.1365-2958.2010.07330.x  
589 (2010).

590 41 Nikaido, H. Structure and mechanism of RND-type multidrug efflux pumps. *Adv*  
591 *Enzymol Relat Areas Mol Biol* **77**, 1-60 (2011).

592 42 Tsukagoshi, N. & Aono, R. Entry into and release of solvents by Escherichia coli in an  
593 organic-aqueous two-liquid-phase system and substrate specificity of the AcrAB-TolC  
594 solvent-extruding pump. *J Bacteriol* **182**, 4803-4810 (2000).

595 43 White, D. G., Goldman, J. D., Demple, B. & Levy, S. B. Role of the acrAB locus in  
596 organic solvent tolerance mediated by expression of marA, soxS, or robA in  
597 Escherichia coli. *J Bacteriol* **179**, 6122-6126 (1997).

598 44 Eicher, T. *et al.* Coupling of remote alternating-access transport mechanisms for  
599 protons and substrates in the multidrug efflux pump AcrB. *Elife* **3**,  
600 doi:10.7554/eLife.03145 (2014).

601 45 Vargiu, A. V., Ruggerone, P., Opperman, T. J., Nguyen, S. T. & Nikaido, H. Molecular  
602 mechanism of MBX2319 inhibition of Escherichia coli AcrB multidrug efflux pump  
603 and comparison with other inhibitors. *Antimicrob Agents Chemother* **58**, 6224-6234,  
604 doi:10.1128/AAC.03283-14 (2014).

605 46 Takatsuka, Y. & Nikaido, H. Threonine-978 in the transmembrane segment of the  
606 multidrug efflux pump AcrB of Escherichia coli is crucial for drug transport as a  
607 probable component of the proton relay network. *J Bacteriol* **188**, 7284-7289,  
608 doi:10.1128/JB.00683-06 (2006).

609 47 Case, D. A. *et al.* AMBER 12. *University of California, San Francisco* (2012).

610 48 Nissink, J. W. *et al.* A new test set for validating predictions of protein-ligand  
611 interaction. *Proteins* **49**, 457-471, doi:10.1002/prot.10232 (2002).

612 49 Nakashima, R. *et al.* Structural basis for the inhibition of bacterial multidrug  
613 exporters. *Nature* **500**, 102-106, doi:10.1038/nature12300 (2013).

614 50 Case, D. A. *et al.* The Amber biomolecular simulation programs. *J Comput Chem* **26**,  
615 1668-1688, doi:10.1002/jcc.20290 (2005).

616 51 Jo, S., Kim, T., Iyer, V. G. & Im, W. CHARMM-GUI: a web-based graphical user  
617 interface for CHARMM. *J Comput Chem* **29**, 1859-1865, doi:10.1002/jcc.20945  
618 (2008).

619 52 Dickson, C. J. *et al.* Lipid14: The Amber Lipid Force Field. *J Chem Theory Comput* **10**,  
620 865-879, doi:10.1021/ct4010307 (2014).

621 53 Hopkins, C. W., Le Grand, S., Walker, R. C. & Roitberg, A. E. Long-Time-Step  
622 Molecular Dynamics through Hydrogen Mass Repartitioning. *J Chem Theory Comput*  
623 **11**, 1864-1874, doi:10.1021/ct5010406 (2015).

624 54 Maier, J. A. *et al.* ff14SB: Improving the Accuracy of Protein Side Chain and Backbone  
625 Parameters from ff99SB. *J Chem Theory Comput* **11**, 3696-3713,  
626 doi:10.1021/acs.jctc.5b00255 (2015).

627 55 Daidone, I. & Amadei, A. Essential dynamics: foundation and applications. *WIREs*  
628 *Comput Mol Sci* **2**, 762-770, doi:10.1002/wcms.1099 (2012).

629 56 Garcia, A. E. Large-amplitude nonlinear motions in proteins. *Phys Rev Lett* **68**, 2696-  
630 2699, doi:10.1103/PhysRevLett.68.2696 (1992).



- 57 Thomas, J. R., Gedeon, P. C., Grant, B. J. & Madura, J. D. LeuT conformational  
sampling utilizing accelerated molecular dynamics and principal component analysis.  
*Biophys J* **103**, L1-3, doi:10.1016/j.bpj.2012.05.002 (2012).
- 58 Gedeon, P. C., Thomas, J. R. & Madura, J. D. Accelerated molecular dynamics and  
protein conformational change: a theoretical and practical guide using a membrane  
embedded model neurotransmitter transporter. *Methods Mol Biol* **1215**, 253-287,  
doi:10.1007/978-1-4939-1465-4\_12 (2015).

## Acknowledgements

We thank Mr Daniel Mikolajczyk, IT Systems Administrator of King's College London, for installing and supporting FWB-Lab-Tesla HPC system on the Rahman research group's supercomputer (Tesla Biohealth Lab). This work was funded by Grants from National Biofilm Innovation Centre (POC2-091) and BBSRC (BB/T007737/1). We are also thankful to Dr Mark Laws for proofreading an earlier version of the manuscript.

## Author contribution

SJ, KMR and JMS conceived the study. SJ designed and performed the study and wrote the manuscript. SJ contributed to data analysis. SJ wrote the manuscript, KMR and JMS edited the manuscript.

## Conflicts of Interests

The authors have no conflict of interest to declare.

## Data Availability Statement

All data generated or analysed during this study are included in this published article (and its Supplementary Information files).

**Table 1.** Distances with the highest density for each pair of positions in TM helices of ligand-free, PAβN-bound and TET-bound states of MexB.

Distance (Å) with highest density during MD		MexB			MexB-PAβN			MexB-TET		
TM helix	Residues	Access	Binding	Release	Access	Binding	Release	Access	Binding	Release
TM2-TM10	Glu346_Asp923	28.99	28.73	25.99	26.53	26.39	26.82	26.54	28.74	27.35
TM11-TM2	Thr976_His338	27.92	26.14	29.57	28.17	25.51	29.54	27.92	26.65	29.69
TM10-TM11	Lys939_Thr976	12.38	13.09	11.83	13.59	12.97	12.00	12.96	10.67	11.42
TM4-TM11	Asp407_Thr976	7.97	6.66	6.45	7.04	6.47	6.51	7.37	6.87	6.62
TM4-TM10	Asp408_Asp923	28.59	28.56	26.51	29.30	27.89	26.48	29.36	28.08	26.76
TM10-TM11	Asp923_Thr976	28.1	58.63	57.68	28.39	58.71	56.51	28.02	58.52	56.76
TM4-TM2	Asp408_His338	28.4	25.58	27.21	27.36	25.26	27.03	27.42	25.59	27.11
TM7t-TM10	Asp566_Asp923	10.64	8.75	10.12	13.51	8.74	10.52	10.21	8.52	10.96
TM7t-Binding Site	Asp566_Phe617	24.53	22.04	22.51	22.55	22.89	23.06	21.98	22.78	22.85
Postulate gate	Gln125_Tyr757	9.20	9.10	18.45	9.64	7.90	15.97	8.44	7.67	16.24
Cleft	Phe664_Arg716	11.32	13.95	8.86	11.00	12.41	8.64	11.95	10.07	9.53

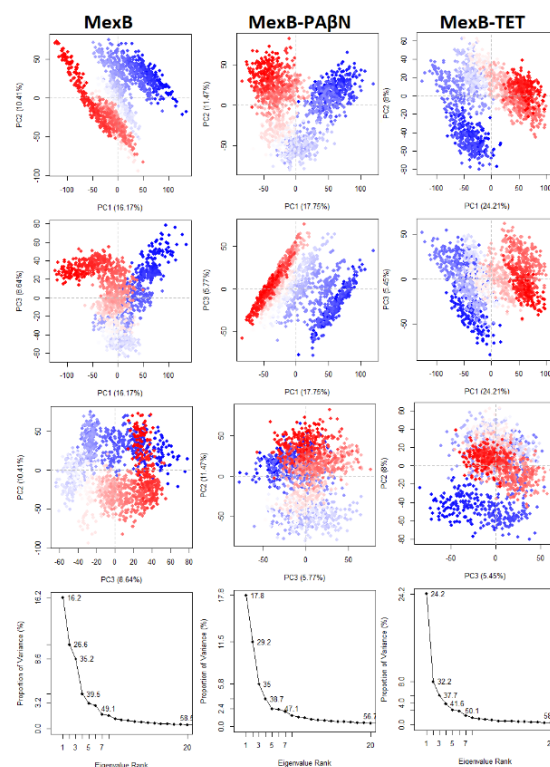


**Figure 1.** Rows 1-3) PCA results for MexB in free form and in complex with PA $\beta$ N and TET trajectories with instantaneous conformations (trajectory frames) coloured from blue to red in order of time. Row 4) The rank ordering of the eigenvalues of the covariance matrix. Eigenvalue spectrum; Results obtained from diagonalization of the atomic displacement correlation matrix of C $\alpha$  atom coordinates from the first snapshot structures. Inset shows histograms for the projection of the distribution of structures onto the first three principal components.

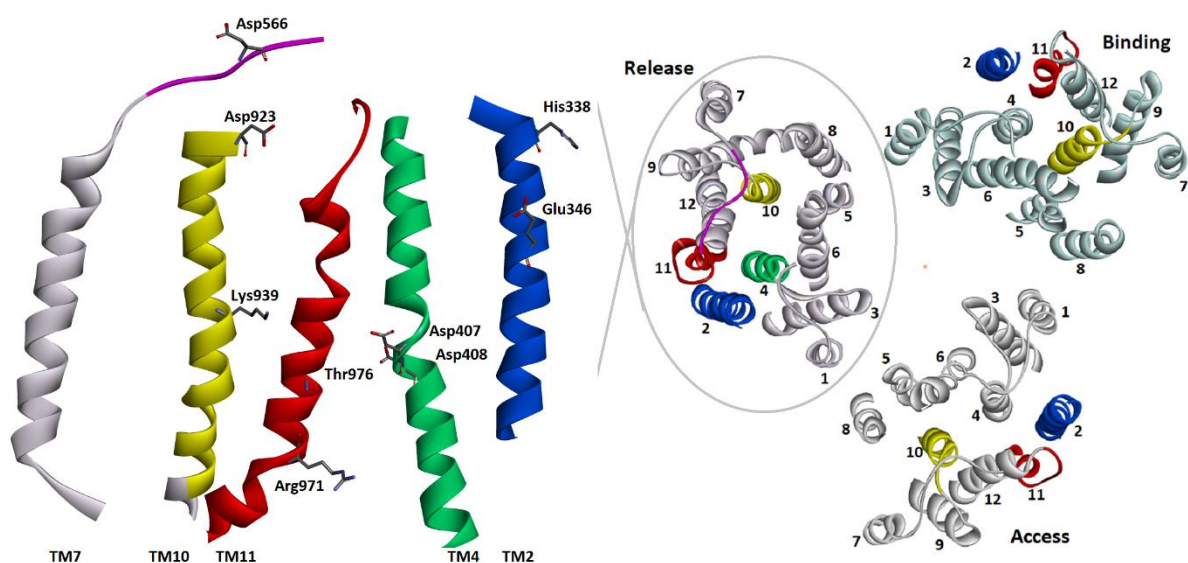


**Figure 2.** Periplasmic top view of a ribbon representation of the protomers is represented in right panel. The label numbers indicate the transmembrane helix numbers (TMx). The individually colored helices include the protonated residues in each protomer. A side view of the transmembrane domain with protonating residues marked is provided in the left panel as well.

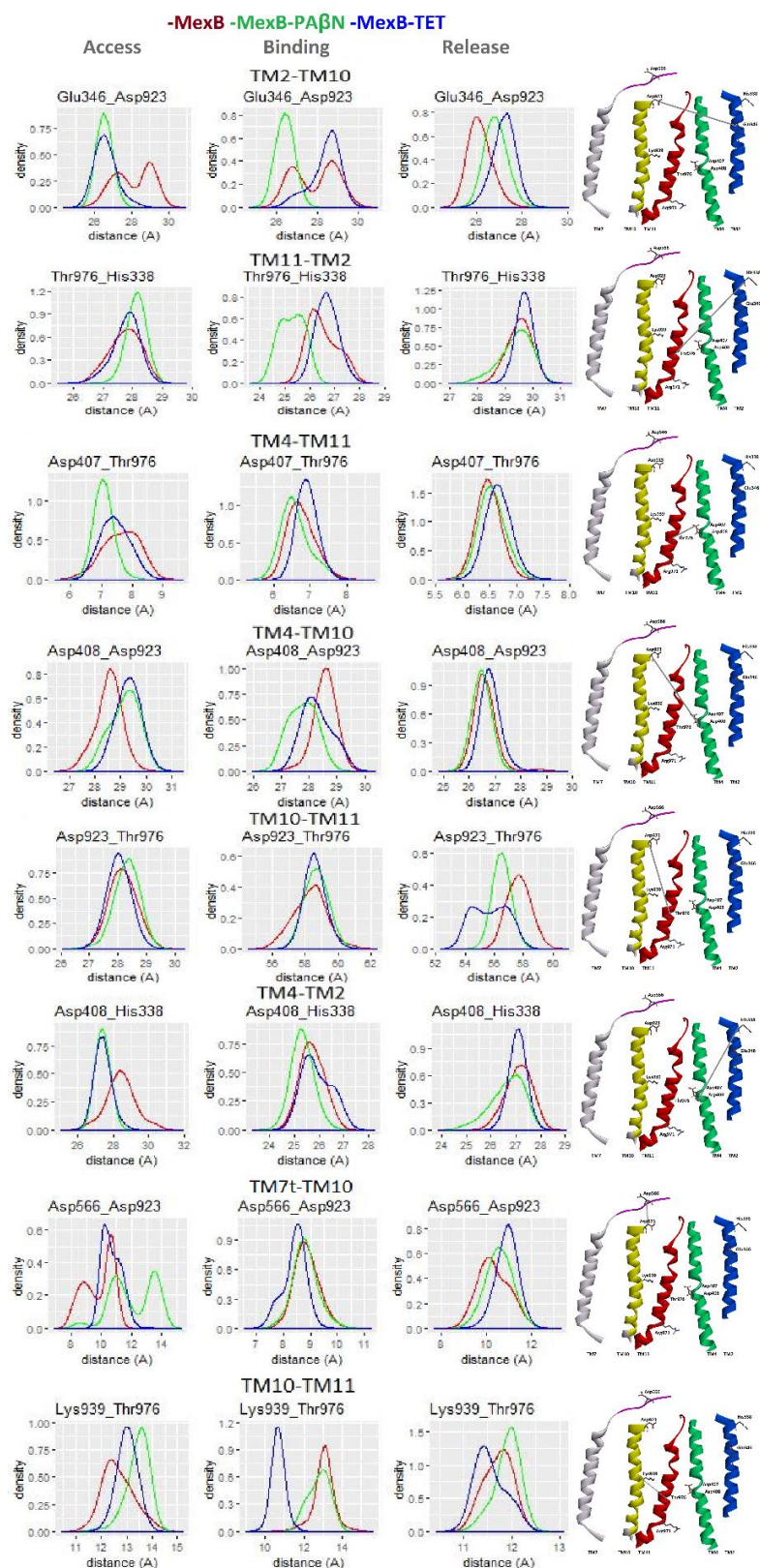


**Figure 3.** Ligand-dependent conformational changes of MexB in the transmembrane regions (TM2, 4, 10 and 11). Distance distributions showing density versus distance between identical positions in the labelled structure. Distance distributions for each pair were obtained in the ligand-free (red), PAβN-bound (green) and TET-bound (blue) systems. For clarity, TM helices are shown in expanded form in the right-hand panel



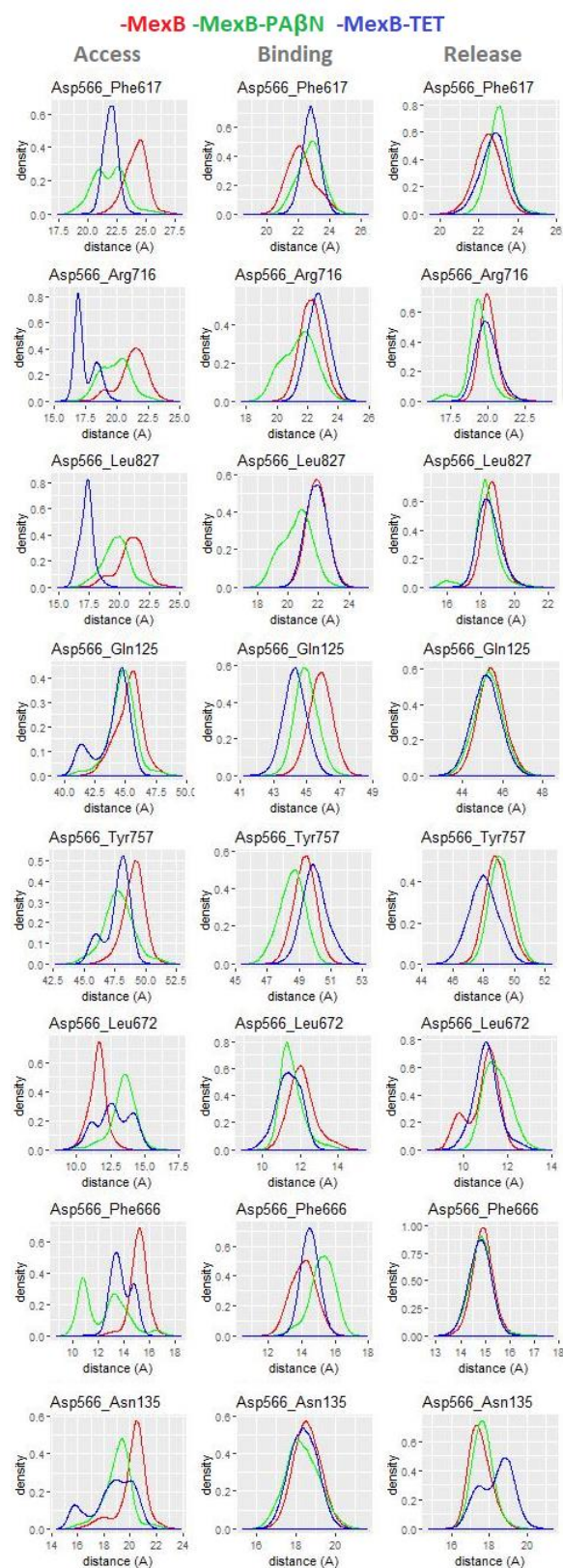


**Figure 4.** Ligand-dependent conformational changes in the distance between Asp566 in the transmembrane regions to the key residues of multi-binding site of MexB. Distance distributions show the density versus distance between identical amino acid positions and Asp566. Distance distributions were obtained in the ligand free (red), PAβN-bound (green) and TET-bound (blue) systems.

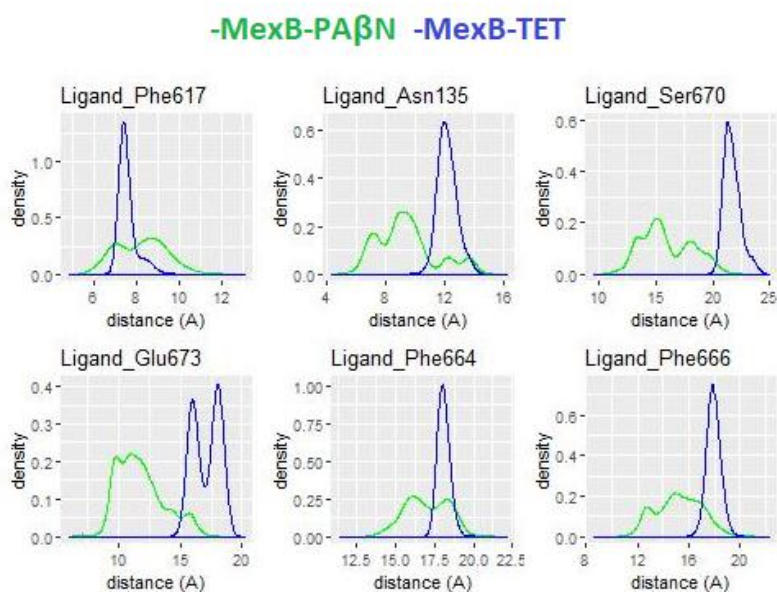


**Figure 5.** Density of distance distribution in terms of the distance between the ligands and diverse key residues of passageway of multi-binding site in binding protomer of MexB-PAβN (green) and MexB-TET (blue) complexes as calculated from MD trajectories. Distance distributions show density versus distance between identical positions from the bound ligands.

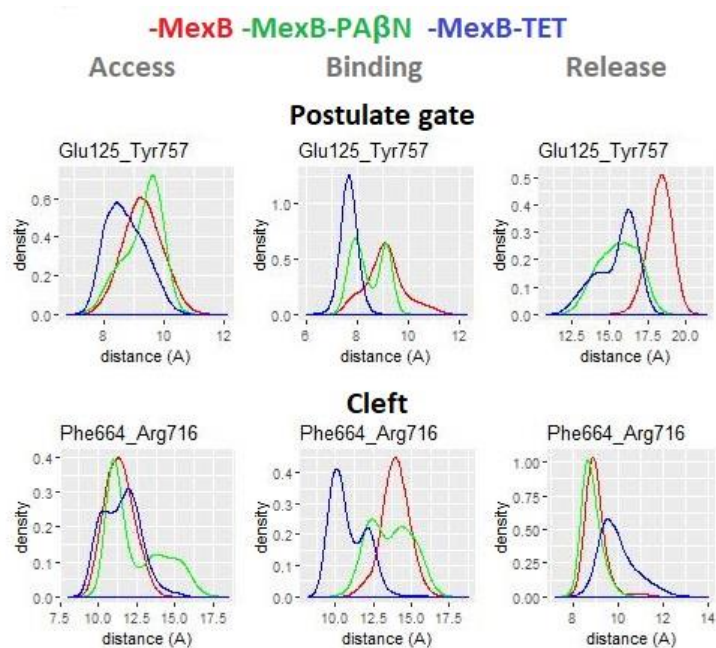


**Figure 6.** Density of distance distribution between the postulated gate residues and cleft residues in diverse protomers of MexB (red), MexB-PAβN (green) and MexB-TET (blue) complexes as calculated from MD trajectories. Distance distributions depict the density of a distance versus distance between identical position of Glu125 and Tyr757 and Phe664 and Arg716 as representative residues of postulated gate and cleft in diverse monomers of the different systems.